Reduced-Order Aerodynamic Modeling Based on CFD Frequency Responses from Multisine Inputs

Jared A. Grauer,* Josiah M. Waite,† and Bret K. Stanford‡
NASA Langley Research Center, Hampton, Virginia, 23681

A system identification analysis was performed to determine a reduced-order model (ROM) of a computational fluid dynamics (CFD) solver in support of linear aeroservoelastic model development and feedback control design. The approach was applied to the CFD code called FUN3D for the half-span wind tunnel test article used in the NASA-Boeing collaboration named the Integrated Adaptive Wing Technology Maturation (IAWTM) project. In a transonic flow condition, multiple inputs (11 structural mode displacements and 3 control surface deflections) were simultaneously excited with orthogonal phase-optimized multisines while multiple outputs (the corresponding 14 generalized aerodynamic forces) were recorded. From these recorded times series, the matrix of frequency responses was computed and subsequently fit using rational function approximations (RFAs). It was found that the entire (14×14) matrix of frequency responses could be determined from a single CFD run and that results generally followed trends predicted using other methods. Differences were attributed to the modeling fidelity and nonlinearities from structural mode and control surface interactions at higher reduced frequencies. More accurate fits of the RFAs to the frequency response data were obtained by making two CFD runs, one with only structural mode excitations and one with only control surface excitations, which reduced the degree of nonlinearity in the modeling data.

I. Nomenclature

$\bar{c}$	=	mean aerodynamic chord, ft
$\mathbb{I}$	=	identity matrix
j	=	imaginary number = $\sqrt{-1}$
k	=	reduced frequency
n_u, n_y	=	number of inputs and outputs
$\Re$	=	real part of number
R^2	=	coefficient of determination
t	=	time, s
V	=	airspeed, ft/s
x, y, z	=	body-axis coordinates, ft
Δ	=	perturbation
Δt	=	sampling period, s
ω	=	radian frequency, rad/s
†	=	complex conjugate transpose
$^{-1}$	=	matrix inverse
$\hat{}$	=	estimate

*Research Engineer, Dynamic Systems and Control Branch, MS 308, Associate Fellow AIAA.
†Research Engineer, Aeroelasticity Branch, MS 340, Member AIAA.
‡Research Engineer, Aeroelasticity Branch, MS 340, Associate Fellow AIAA.

II. Introduction

Computational fluid dynamics (CFD) flow solvers coupled to structural models offer higher-fidelity aeroelastic modeling capability than first-principles approaches or linear panel code solutions, particularly in the transonic flow regime where nonlinearities may arise. However, it is not generally feasible to use CFD solutions directly for initial aeroelastic analysis and control design before testing a vehicle or model due to the high computational costs and incompatibility with standard modeling tools such as the state-space approach. As a result, lower-fidelity aerodynamic solutions that are rapidly constructed and easily incorporated into aeroelastic analysis tools are often preferred for these applications.

When linear aerodynamic solutions cannot meet modeling accuracy requirements, a different approach is to perform a system identification analysis on the CFD code using the recorded aerodynamic input (prescribed structural mode displacements and control surface deflections) and output (generalized aerodynamic forces) data. The goal is a reduced-order model (ROM) that approximates the CFD outputs to specific inputs under certain conditions to a reasonable level of accuracy, and given in a form that can be easily applied to linear analysis and feedback control design methods.

Aerodynamic ROMs have been identified using a variety of excitations on the structural modes and control surface deflections including sinusoids, impulses, squares waves (steps, doublets, or multisteps), frequency sweeps, random excitations, and other waveforms [1–4]. However, these single-input designs require long durations of computation time or multiple CFD runs to achieve solutions for systems with multiple inputs, such as aircraft. Alternatively, orthogonal excitations on multiple simultaneously-moved inputs have included Gaussian functions [2] and Walsh functions (orthogonal square waves) [4–6], which can generate data for identifying the entire model from a single CFD run and therefore reduce computation costs. The eigenvalue realization algorithm (ERA) [7] is often employed with these inputs to directly realize aerodynamic ROMs in state-space form directly from recorded time series data. Many of these techniques are compiled into the software package called AEROM, which is described and demonstrated in Ref. [6] and the references therein.

A similar but different approach is pursued in this paper for identifying ROMs of CFD codes. Multiple inputs are simultaneously excited using orthogonal phase-optimized sinusoids instead of Walsh functions. From the recorded input and output data from a single CFD run, the frequency response matrix is computed as a ratio of output to input Fourier transform data. A model structure is then determined and parameter estimation techniques are applied to fit a rational function approximation (RFA) to the frequency response data. The RFA then constitutes a ROM of the aerodynamics that can be coupled to other dynamics to form a state-space model of the system for analysis and control design [8]. The approach is applied to the CFD code called FUN3D [9, 10] and a flexible half-span wind tunnel test article, set to a transonic flow condition, used in the NASA-Boeing collaboration called the Integrated Adaptive Wing Technology Maturation (IAWTM) project. Results from this study and other work [11, 12] will be used to support the aeroservoelastic (ASE) modeling and feedback control design for upcoming tests of the IAWTM wind tunnel test article.

The paper is hereafter organized as follows. The wind tunnel test article, structural model, and aerodynamic models used in the IAWTM project are discussed in Section III. An overview of the ASE model and equations of motion is summarized in Section IV. The system identification approach for obtaining a simplified aerodynamic model of the CFD flow solver is described in Section V. Modeling results are presented in Section VI. Conclusions are discussed in Section VII.

III. Description of IAWTM

The NASA Advanced Air Transport Technology (AATT) project seeks to develop advanced next-generation subsonic commercial transports with higher fuel economy and lower emissions and noise signatures [13]. The resulting high aspect ratio, low-weight aircraft designs have increased the need for aeroelastic modeling and flight control design. The IAWTM project was created as a collaboration between NASA and Boeing to identify, develop, and demonstrate new technologies towards these goals.

To test and demonstrate these new technologies, a wind-tunnel test in the NASA Langley Research Center (LaRC) Transonic Dynamics Tunnel (TDT) is scheduled for the year 2021. A half-span test article will be installed against the tunnel sidewall and a variety of tests will be conducted at subsonic and transonic flow conditions. ASE models and feedback control designs are in development for active flutter suppression (AFS), maneuver load alleviation (MLA), gust load alleviation (GLA), and drag reduction [11, 12, 14, 15].

A. Wind Tunnel Test Article

A computer rendering of the IAWTM test article showing the component subassemblies is given in Fig. 1. The design is based on the Common Research Model (CRM-13), described in Ref. [16], but is a half-span and aeroelastically-scaled version where the wing aspect ratio has been increased from 9 to 13.5. The IAWTM has a 12.9 ft half-wing span, 2.04 ft mean aerodynamic chord, and 13.3 ft fuselage length. The wing is composed of a wing spar, ribs, actuators, instrumentation, and a flow-through engine nacelle. A tail section is not installed. The wing connects to a mounting structure inside the fuselage skin, which can be attached to the tunnel load balance.

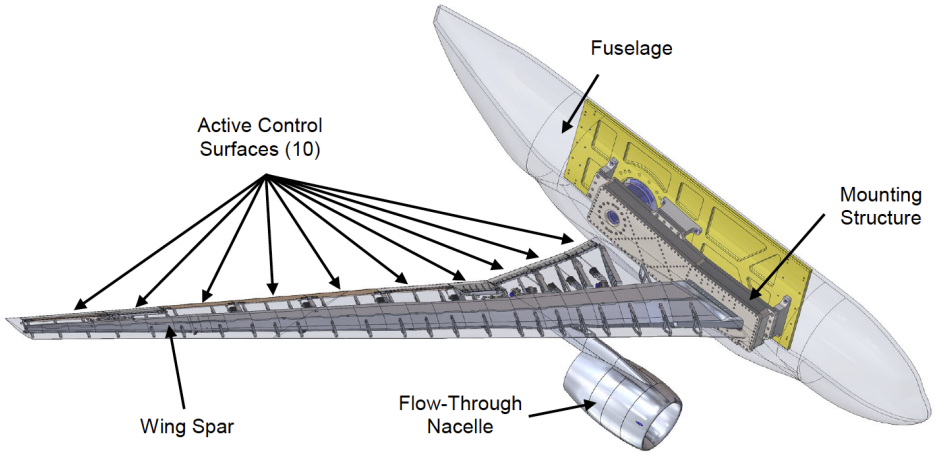

Fig. 1 Cutaway rendering of component subassemblies.

The test article includes 10 independently-actuated control surfaces along the trailing edge of the wing, as shown in Fig. 1 and depicted by the instrumentation layout in Fig. 2. The surfaces labeled δ_f are miniature plane flaps, which are controlled by electric servo motors for lower-frequency applications such as MLA and drag optimization. The surfaces labeled δ_a are the ailerons, which are controlled by hydraulic actuators for use in higher-frequency AFS control laws. Potentiometers were installed at the hinges to measure control surface deflections.

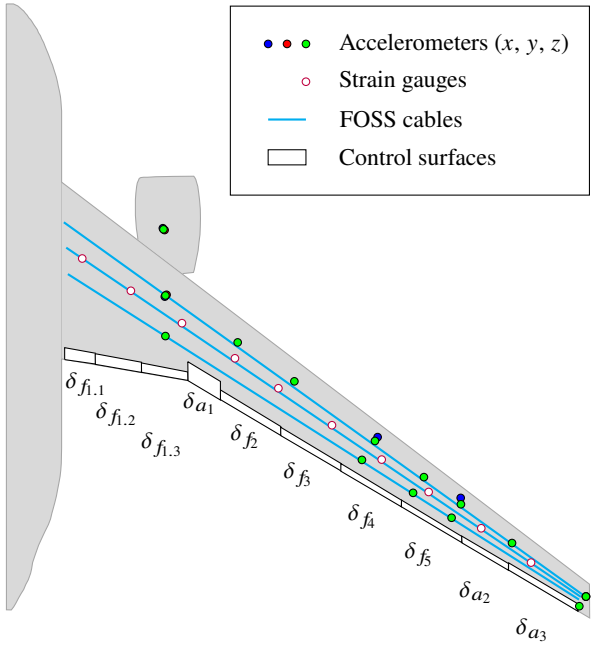

Fig. 2 Instrumentation layout for the IAWTM test article.

Also shown in Fig. 2 are the locations of several sensors used for measuring the response of the wing. At 10 locations along the span, shown by the white circles, are conventional strain gauges configured in a full-bridge setup, with two gauges on the top and two gauges on the bottom surfaces of the wing spar, totaling 20 measurements. In addition to these conventional strain measurements, there are three fiber-optic strain sensor (FOSS) cables, shown by the blue lines, on the upper surface of the spar. The forward, middle, and aft FOSS cables contain 40, 39, and 38 gratings, respectively, that provide 117 discrete strain measurements in total. Also shown are the locations of 22 accelerometers (some of which are colocated): 5 in the x direction, 3 in the y direction, and 14 in the z direction.

B. Structural Dynamics Model

The finite element model (FEM) describing the structural dynamics of the IAWTM wind tunnel test article was constructed using MSC Nastran®. The model had 38,667 grid points that consisted of rigid beam, flexible beam, flat plate, shell, and solid hexahedral elements. This work retained 24 elastic modes, which ranged in frequency from 3.6 to 100 Hz. A free-vibration analysis was used to compute the natural frequencies and the mode shapes, which were normalized to have unit generalized mass. No structural damping was assumed. The equations of motion were solved using a second-order accurate predictor-corrector scheme that was marched in time along with the CFD solver, discussed next. See Refs. [11, 12] for more details about the structural dynamics model.

It was determined, using a trial and error procedure, that only 11 structural modes were needed to accurately model the flutter instability. These modes are listed in Table 1 with the in-vacuo frequencies and descriptions. For this work, only these modes were retained during the modeling. Aeroelastic instabilities involving structural modes 2, 4, and 5 exhibit hump-mode type flutter mechanisms, whereas structural modes 4, 5, and 6 participate in a hard flutter type mechanism [11].

Table 1 Descriptions of retained structural modes.

Mode	Frequency, rad/s	Frequency, Hz	Description
1	22.7	3.6	1st wing vertical bending
2	48.0	7.6	1st fuselage pitch, wing 1st vertical bending
4	69.6	11.1	2nd wing vertical bending
5	94.1	15.0	2nd wing/balance fore/aft bending
6	95.2	15.1	2nd wing vertical bending, fuselage pitch
7	107.5	17.1	1st nacelle pitch, inboard wing 1st torsion
8	151.1	24.0	nacelle lateral
10	184.3	29.3	nacelle lateral, balance axial
13	275.4	43.8	—
14	287.1	45.7	—
18	466.2	74.2	—

C. Aerodynamics Models

The aerodynamics acting on the IAWTM wind tunnel test article were modeled using two numerical codes. The first was the CFD code named FUN3D (Fully Unstructured 3-Dimensional Navier-Stokes), which was developed at NASA Langley Research Center [9, 10]. FUN3D is a node-centered finite-volume unstructured code used to solve the steady and unsteady Reynolds-averaged Navier-Stokes (RANS) equations using a second-order upwind scheme with the Spalart-Allmaras turbulence model. For this work, the CFD mesh was moved at each time step in accordance with structural deformations and control surface deflections. The solutions used 14,618,916 nodes, 3,598,892 tetrahedral cells, 184,622 pyramid cells and 27,598,875 prism cells. See Refs. [11, 12] for more details about the FUN3D solver application to the IAWTM.

The second code used was ZAERO™, which uses a linear panel method [8]. Flat plate elements were used for the wing and pylon, and body elements were used for the fuselage and flow-through engine nacelle. Panels for the wing and nacelle were connected to the structure with an infinite plate spline, and motion of the fuselage body was ignored. See

Ref. [11] for more details about the ZAERO application to the IAWTM.

The panel method results are included in this paper as a comparison for the CFD solution. Reference [11] showed that predictions of flutter onset were in reasonable agreement with each other. For example, at 0.8 Mach, the CFD and panel method predictions of the flutter frequency varied within 0.7% and the flutter dynamic pressure varied within 4%.

IV. Aeroservoelastic Model

A block diagram of the ASE model is shown in Fig. 3. The main components are the aerodynamics, structural dynamics, sensors, actuators, and control laws. The structural dynamics pertain to the linear second-order equations derived from the FEM discussed in Section III.B. The aerodynamics can pertain to the CFD solver or panel code discussed in Section III.C, or an identified ROM. The dashed block is the aeroelastic (AE) model, which couples the structural dynamics and aerodynamics. Additional gust inputs were included in the ASE model but are not shown.

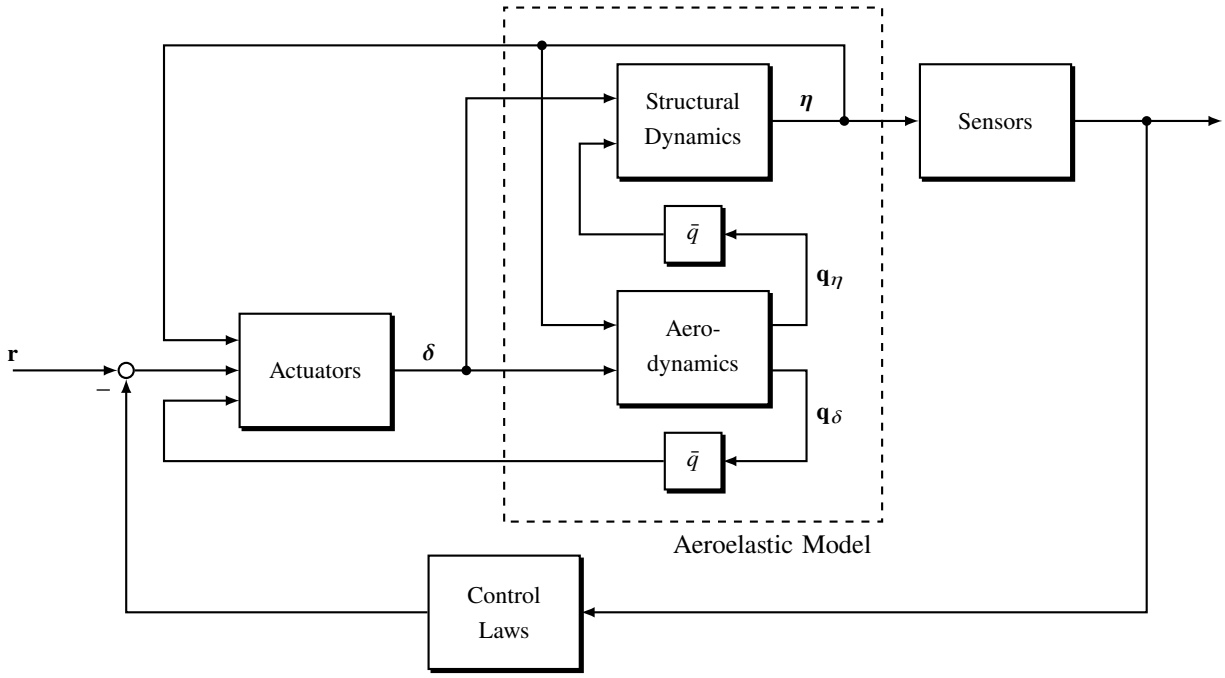

Fig. 3 Block diagram of the aeroservoelastic model.

The inputs to the aerodynamics block are the structural mode displacements $\boldsymbol{\eta}$ and the control surface deflections $\boldsymbol{\delta}$. The outputs of the aerodynamics block are the nondimensional generalized aerodynamic forces (GAFs) $\mathbf{q}_\eta$ and $\mathbf{q}_\delta$. The GAFs are scaled by dynamic pressure $\bar{q}$ and force the structural dynamics and control surface dynamics.

A linear model coupling the actuators, structural dynamics, and aerodynamics can be written succinctly in the frequency domain as [3, 8, 17–21]

$$\mathbf{G}(s)\mathbf{x}(s) = \bar{q}\,\mathbf{q}(s) + \boldsymbol{\tau}_{hm}(s) \tag{1}$$

where

$$s = \sigma + j\omega \tag{2}$$

is the dimensional Laplace variable and

$$\mathbf{x}(s) = \begin{bmatrix} \boldsymbol{\eta}(s) \\ \boldsymbol{\delta}(s) \end{bmatrix} \tag{3}$$

are the aeroelastic degrees of freedom.

On the left side of Eq. (1), the matrix

$$\mathbf{G}(s) = s^2 \begin{bmatrix} \mathbf{M}_{\eta\eta} & \mathbf{M}_{\eta\delta} \\ \mathbf{M}_{\delta\eta} & \mathbf{M}_{\delta\delta} \end{bmatrix} + s \begin{bmatrix} \mathbf{C}_{\eta\eta} & \mathbf{0} \\ \mathbf{0} & \mathbf{0} \end{bmatrix} + \begin{bmatrix} \mathbf{K}_{\eta\eta} & \mathbf{0} \\ \mathbf{0} & \mathbf{0} \end{bmatrix} \tag{4}$$

is composed of generalized mass, damping, and stiffness matrices. The top row corresponds to the structural dynamics and the bottom row corresponds to the control surfaces. The generalized mass matrices $\mathbf{M}_{\eta\delta}$ and $\boldsymbol{M}_{\delta\eta}$ inertially couple the two sets of equations. The ASE models constructed using aerodynamics from ZAERO neglected the $\mathbf{M}_{\delta\eta}$ and $\mathbf{M}_{\delta\delta}$ mass terms, which resulted in irreversible actuators driven only by the actuator commands $\mathbf{r}$ and not by structural or aerodynamic forces. ASE models constructed using aerodynamics from FUN3D additionally neglected $\mathbf{M}_{\eta\delta}$.

The control surface displacements are idealized as being free to rotate. Stiffness and damping matrices for the control surface deflection were applied to the actuator transfer function in the generalized hinge moment vector $\boldsymbol{\tau}_{hm}$ and are therefore not present in the bottom row of Eq. (4). In this way, accelerations cannot be directly induced on the control surface dynamics by the in-vacuo displacements of other control surfaces [19, 20].

On the right side of Eq. (1), the nondimensional GAFs $\mathbf{q}(s)$ can be decomposed into parts acting on the structural dynamics $\mathbf{q}_\eta(s)$ and parts acting on the control surface dynamics $\mathbf{q}_\delta(s)$. Furthermore, these forces can be written as the square transfer function matrix

$$\mathbf{q}(s) = \begin{bmatrix} \mathbf{q}_\eta(s) \\ \mathbf{q}_\delta(s) \end{bmatrix} = \begin{bmatrix} \mathbf{Q}_{\eta\eta}(s) & \mathbf{Q}_{\eta\delta}(s) \\ \mathbf{Q}_{\delta\delta}(s) & \mathbf{Q}_{\delta\delta}(s) \end{bmatrix} \begin{bmatrix} \boldsymbol{\eta}(s) \\ \boldsymbol{\delta}(s) \end{bmatrix} \tag{5}$$

The goal of this paper is to determine models of Eq. (5) from high-fidelity CFD data that can be assembled into a state-space representation of the ASE model for linear control design and analysis. Towards this end, each transfer function submatrix $\mathbf{Q}(s)$ in Eq. (5) can be modeled by a RFA, such as the partial-fraction expansion [8, 21, 22]

$$\mathbf{Q}(p) = \mathbf{A}_0 + p\mathbf{A}_1 + p^2\mathbf{A}_2 + p\mathbf{D}\left(p\mathbb{I} - \mathbf{R}\right)^{-1}\mathbf{E} \tag{6}$$

where

$$p = g + jk \tag{7a}$$

$$= \frac{s\bar{c}}{2V} \tag{7b}$$

The variable p is the nondimensional Laplace variable, which is analogous to the dimensional version in Eq. (2), with real part g and imaginary part

$$k = \frac{\omega\bar{c}}{2V} \tag{8}$$

called the reduced frequency. The fitting of Eq. (6) to frequency response data is done in nondimensional Laplace variables to simplify the expressions and maintain compatibility with the available modeling data. Afterwards, identified ROMs in the form of Eq. (6) are converted back into dimensional Laplace variables for coupling to the structural dynamics equations and assembling the ASE model. Ultimately, the ASE model is expressed in state-space representation for analysis and control design. The matrices $\mathbf{A}_0$, $\mathbf{A}_1$, and $\mathbf{A}_2$ represent aerodynamic stiffness, damping, and apparent mass terms. The matrix $\mathbf{R}$ is diagonal and contains the roots of first-order aerodynamic lag states, with $\mathbf{D}$ and $\mathbf{E}$ being aerodynamic coupling matrices. The coefficient matrices in Eq. (6) are often estimated using least squares to match tabulated GAF data from numerical analyses, after specifying the aerodynamic poles [8, 23, 24]. In other approaches, a nonlinear optimization is performed to determine the coefficient matrices, where various constraints can be applied [23–25]. These approaches are in contrast to the ERA method [7], in which state-space models are fit to impulse response functions obtained from the aerodynamic input-output data [6].

V. System Identification Approach

A. Overview

This section describes the techniques used to identify a ROM for the GAFs, parameterized by Eq. (6) and based on aerodynamic input-output data from a high-fidelity CFD code. As suggested in Refs. [2, 4, 6], the approach was to decouple the aerodynamics block in Fig. 3 (implemented using FUN3D) from the other dynamics and apply system identification procedures to the input and output data. A block diagram for this decoupled system is shown in Fig. 4.

The process began by determining a converged solution for the aerodynamic flow field, having steady-state trimmed values $\boldsymbol{\eta}_0$ and $\boldsymbol{\delta}_0$ for the structural modes and control surface deflections. Small perturbation signals $\Delta\boldsymbol{\eta}(t)$ and $\Delta\boldsymbol{\delta}(t)$ were designed and added to the steady-state values to excite the dynamics of interest, as described in Section V.B. Using

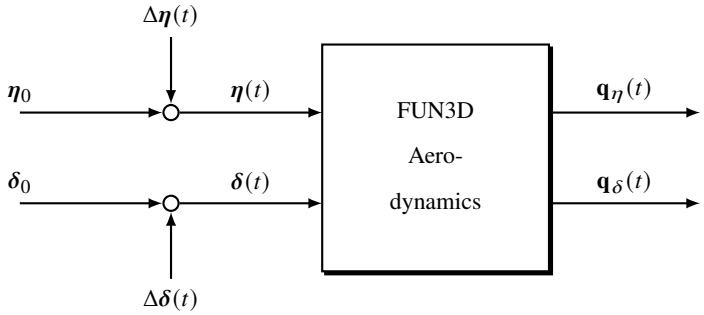

Fig. 4 Block diagram of the aerodynamics model used for system identification.

a procedure summarized in Section V.C, frequency responses were computed from recorded time series of the FUN3D inputs and outputs. Then using the standard least-squares procedure described in Section V.D, a model of the form in Eq. (6) was identified for each frequency response.

For this system identification analysis, the inputs were the 11 retained structural modes and 3 aileron control surfaces, and the outputs were the corresponding 14 nondimensional GAFs. These terms are combined as the aerodynamic inputs and outputs

$$\mathbf{u}(t) = \begin{bmatrix} \boldsymbol{\eta}(t) \\ \boldsymbol{\delta}(t) \end{bmatrix} \qquad \mathbf{y}(t) = \begin{bmatrix} \mathbf{q}_\eta(t) \\ \mathbf{q}_\delta(t) \end{bmatrix} \tag{9}$$

with analogous terms $\mathbf{u}_0$, $\mathbf{y}_0$, $\Delta\mathbf{u}(t)$, and $\Delta\mathbf{y}(t)$ for the trim and perturbation parts. The other structural modes and miniature plane flap control surfaces were kept at zero.

The input design, Fourier transforms, and parameter estimation discussed in the following sections used a software package called System IDentification Programs for AirCraft (SIDPAC) [26], which was developed at NASA Langley Research Center and is associated with Ref. [27].

B. Experiment Design

The excitations added to steady-state values of the aerodynamics inputs were orthogonal phase-optimized multisines [26, 27]. These multisines have the form

$$\Delta u_j(t) = \sum_{m \in S_j} a_m \sin\left(\frac{2\pi m}{T} t + \phi_m\right) \tag{10}$$

for each input, $j = 1, 2, \ldots, n_u$. Equation (10) represents a summation of mutually orthogonal sinusoids that are each the mth harmonic of the fundamental frequency $1/T$ Hz for the fundamental period T seconds.

The harmonics m and frequencies m/T, specified over a bandwidth of interest, are assigned to each of the inputs, usually in an alternating manner for balanced participation of the inputs over frequency. Each input has a subset of M_j harmonics grouped in the set S_j. The coefficients a_m are selected to tailor the excitation power spectra. Afterwards, a Simplex optimization is performed to determine phase angles ϕ_m for each input that minimize a relative peak factor (RPF) index [27]. The phase angles for each input are then shifted until the corresponding input starts and stops at zero.

There are several benefits to using these multisine excitations for aerodynamic ROM identification. Similar to Walsh functions or staggered pulses [4], these multisines are mutually orthogonal. The value of orthogonal inputs is that instead of running a separate CFD case for each individual input, a single run can be performed where all the inputs are applied simultaneously without correlating the modeling data. Another benefit of multisines is that the range of frequencies are chosen and the power spectra designed to only excite the dynamics of interest for modeling. Moreover, the phase angle optimization creates inputs that are relatively small in amplitude, which is useful for creating small-perturbation responses for linear modeling. Starting the inputs at zero and using sinusoids also encourages the development of the steady-state responses, which are used for frequency response estimation in the following section.

C. Frequency Response Analysis

To compute frequency responses between recorded input and output data, the first step is to transform the data into the frequency domain using the finite-time Fourier transform

$$u_j(j\omega_m) = \int_0^T \Delta u_j(t)\, e^{-j\omega_m t}\, dt \qquad\qquad y_i(j\omega_m) = \int_0^T \Delta y_i(t)\, e^{-j\omega_m t}\, dt \tag{11}$$

for $j = 1, 2, \ldots, n_u$, $i = 1, 2, \ldots, n_y$, and $m \in S_1 \cup S_2 \cup \ldots \cup S_{n_u}$. This step was performed using the chirp-z function implemented in SIDPAC. The second step is to compute the frequency response matrix $\mathbf{Q}(j\omega_m)$ for Eq. (5), which can be done as ratios of the output Fourier transforms to the input Fourier transforms. Individual frequency responses in this matrix are

$$Q_{ij}(j\omega_m) = \frac{y_i(j\omega_m)}{u_j(j\omega_m)} \tag{12}$$

This method for computing the frequency responses assumes that the system under test is linear and that the response data is in steady-state oscillation. Nonlinearities, transient responses, unmodeled inputs, and low signal-to-noise ratios will increase the scatter of the frequency response estimate. Note that the computations in Eqs. (11) and (12) are only performed at the discrete frequencies ω_m in the multisine inputs. This selection reduces the amount of computation compared to spectral estimation techniques and eliminates analyst-selected tuning parameters. See Refs. [26–28] and references therein for more information on this technique, as well as applications to wind tunnel and flight test data.

D. Parameter Estimation

The frequency responses $\mathbf{Q}(j\omega_m)$ can then be nondimensionalized as $\mathbf{Q}(jk_m)$ and fit with RFAs such as in Eq. (6). Using a conventional least-squares approach, the analyst typically selects the aerodynamic roots b_l for $l = 1, 2, \ldots, n_l$ and forms the matrix

$$\mathbf{R} = \begin{bmatrix} b_1 & 0 & \ldots & 0 \\ 0 & b_2 & \ldots & 0 \\ \vdots & \vdots & \ddots & \vdots \\ 0 & 0 & \ldots & b_{n_l} \end{bmatrix} \tag{13}$$

Guidance for selecting the number and location of these roots can be found, for example, in Ref. [8]. For a single-input single-output transfer function, Roger's form [21, 22] for Eq. (6) simplifies to

$$Q_{ij}(p) = a_0 + a_1 p + a_2 p^2 + \sum_{l=1}^{n_l} a_{2+l} \frac{p}{p + b_l} \tag{14}$$

where matrices have been reduced to scalars, and where the **D** and **E** matrices in Eq. (6) have been combined into the a_{2+n_l} coefficients.

By rearranging Eq. (14), the least-squares problem

$$\mathbf{z} = \mathbf{X}\boldsymbol{\theta} + \mathbf{v} \tag{15a}$$

is formed for each frequency response, where

$$\mathbf{z} = \begin{bmatrix} Q_{ij}(jk_1) \\ Q_{ij}(jk_2) \\ \vdots \\ Q_{ij}(jk_{M_j}) \end{bmatrix} \tag{15b}$$

$$\mathbf{X} = \begin{bmatrix} 1 & jk_1 & -k_1^2 & jk_1/(jk_1 + b_1) & jk_1/(jk_1 + b_2) & \ldots & jk_1/(jk_1 + b_{n_l}) \\ 1 & jk_2 & -k_2^2 & jk_2/(jk_2 + b_1) & jk_2/(jk_2 + b_2) & \ldots & jk_2/(jk_2 + b_{n_l}) \\ \vdots & \vdots & \vdots & \vdots & \vdots & \ddots & \vdots \\ 1 & jk_{M_j} & -k_{M_j}^2 & jk_{M_j}/(jk_{M_j} + b_1) & jk_{M_j}/(jk_{M_j} + b_2) & \ldots & jk_{M_j}/(jk_{M_j} + b_{n_l}) \end{bmatrix} \tag{15c}$$

$$\boldsymbol{\theta} = \begin{bmatrix} a_0 \\ a_1 \\ a_2 \\ a_3 \\ a_4 \\ \vdots \\ a_{2+n_l} \end{bmatrix} \tag{15d}$$

and where $\mathbf{v}$ is a vector of modeling residuals. The terms $\mathbf{z}$, $\mathbf{X}$, and $\mathbf{v}$ are complex valued, whereas $\boldsymbol{\theta}$ is real valued.

Equation (15) can be solved for the model parameters that minimize the least-squares cost function

$$J(\boldsymbol{\theta}) = \frac{1}{2} \sum_{m=1}^{M_j} \mathbf{v}(jk_m)^\dagger \mathbf{v}(jk_m) \tag{16}$$

which are the optimal parameter estimates [27]

$$\hat{\boldsymbol{\theta}} = \left[\Re \left(\mathbf{X}^\dagger \mathbf{X} \right) \right]^{-1} \Re \left(\mathbf{X}^\dagger \mathbf{z} \right) \tag{17}$$

This procedure is repeated to determine the coefficients in Eq. (15d) for each frequency response. Afterwards, these estimated coefficients are assembled as the matrix form of the RFA in Eq. (6).

The covariance matrix quantifying the uncertainties in the parameter estimates is

$$\mathrm{cov}(\hat{\boldsymbol{\theta}}) = \sigma^2 \left[\Re \left(\mathbf{X}^\dagger \mathbf{X} \right) \right]^{-1} \tag{18}$$

where the equation-error covariance σ^2 is estimated as the mean square of the residuals. The square root of the diagonal covariance elements are the parameter standard errors. Because the modeling residuals in this application are due to model structure deficiency in Eq. (14), rather than measurement noise assumed in least-squares theory, the standard errors predicted by Eq. (18) are expected to be optimistic.

VI. Results

A. Experiment Design

The FUN3D simulation was set for the conditions of 0 deg angle of attack, 0.8 Mach, 276 lbf/ft^2 dynamic pressure, and 439 ft/s airspeed. To establish a trimmed aerodynamic flow solution, a multiple-step procedure was used. First, the converged steady-state solution for a rigid wing ($\boldsymbol{\eta}$ and $\boldsymbol{\delta}$ constrained to be zero) was obtained. In Fig. 5, which shows a time history of $\eta_1(t)$, this solution corresponds to the initial condition at time $t = 0$ s. Second, the structural stiffness in the wing was enabled and critical damping was artificially added to the structure. This step allowed the flow field to adjust to the static aeroelastic solution, which settled by about 0.3 s. Third, the sampling rate was adjusted to 400 Hz ($\Delta t = 0.0025$ s) for modeling and transients were allowed to settle. Additional parameters for other analyses outside the scope of this paper were also adjusted at this point. Having obtained an adequate trim solution, the multisine excitations began at approximately 3.8 s.

The multisine design for the 14 inputs is summarized by Table 2. The time duration was selected as $T = 20$ s, which was an adequate compromise between the computation time required to run the maneuver and data length to achieve multiple cycles of steady-state data. This selection also set the frequency resolution of the input at $1/T = 0.05$ Hz. No attempt was made to adjust the excitation duration. The CFD runs with this input ran on a cluster of 1250 cores and took 18 hours to complete.

The harmonics were assigned to the inputs in a staggered and alternating manner to balance the input power spectra. The harmonics spanned the frequencies m/T between 0.25 – 80 Hz (reduced frequencies between 0.0037 – 1.2), which encompassed the retained structural modes listed in Table 1. With 14 inputs and 20 s of excitation over this bandwidth, each input had 114 harmonic frequencies, which were spaced every 0.7 Hz. In total, 1596 harmonic frequencies were applied by the inputs.

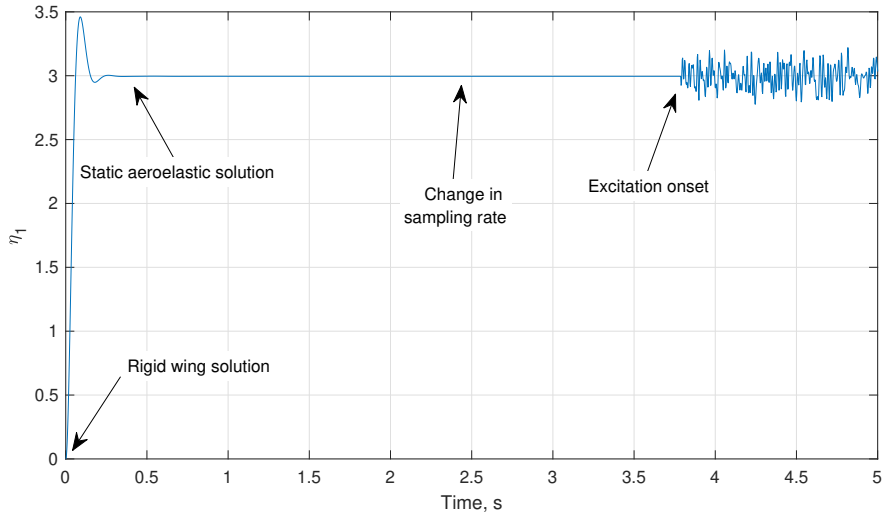

Fig. 5 Example trimming procedure and excitation onset.

As mentioned above, the sampling rate for modeling was 400 Hz. The ratio of the Nyquist rate to the highest retained structural mode natural frequency was about 2.7. Although this value was larger than the theoretical minimum of 1.0, this sampling rate did not meet general guidelines for system identification from flight test data given in Ref. [27], which recommends a minimum ratio of 25. However, measurement noise and other errors usually present in flight test data were not simulated, which allowed the sampling rate to be traded for lower computational costs. Results discussed later indicated 400 Hz was an adequate sampling rate.

The coefficients a_m were selected to be relatively small and have uniform power spectra. The aileron excitations $\Delta\delta_{a_1}$, $\Delta\delta_{a_2}$, and $\Delta\delta_{a_3}$ were scaled for amplitudes of about 2.0, 1.5, and 1.0 deg amplitudes, respectively, based on past experience with wind tunnel tests and flight tests. The scalings were applied in this manner because the outboard control surfaces were generally more effective at exciting the structural modes than the inboard control surfaces. Less intuition was available for selecting the amplitudes of the structural mode inputs. Instead, an ASE model (as shown in Fig. 3), constructed using RFAs identified from the panel code, was simulated to obtain structural mode responses to the aileron control surface excitations. The structural mode input amplitudes for the CFD solver were then sized according to these response levels.

The RPF values listed in Table 2, resulting from the Simplex optimization for the multisine phase angles, were relatively high compared to other multisines designed for flight tests and flight dynamics applications [27, 28]. However, RPF values are generally higher for aeroelastic testing, where many more harmonic frequencies are applied per input to have a large excitation bandwidth [29–31].

Figure 6(a) shows the aerodynamic inputs supplied to the FUN3D CFD solver. As described in Section V.B, the first 3.8 s of simulation data were used to trim the aerodynamic solution. Afterwards, multisines were simultaneously applied to the 14 inputs for 20 s. The markers in these plots are colored to indicate the set of multisine frequencies S_j. This color coding will be used in other plots of the results, where applicable. The GAF outputs from FUN3D are shown in Fig. 6(b). The step changes in the GAFs around 2.4 s coincided with the change in sampling rate but were due to restarting the solution without extra conditions used for other aeroelastic analyses.

Table 2 Multisine input design for 14 inputs, $T = 20$ s.

Number j	Input u_j	Harmonics m	Frequencies m/T, Hz	Power a_m	RPF
1	η_1	$5, 19, \ldots, 1587$	$0.25, 0.95, \ldots, 79.35$	0.0937	1.82
2	η_2	$10, 24, \ldots, 1592$	$0.5, 1.2, \ldots, 79.6$	0.0937	1.90
3	η_4	$15, 29, \ldots, 1597$	$0.75, 1.45, \ldots, 79.85$	0.0937	1.90
4	η_5	$6, 20, \ldots, 1588$	$0.3, 1.0, \ldots, 79.4$	0.0222	1.88
5	η_6	$11, 25, \ldots, 1593$	$0.55, 1.25, \ldots, 79.65$	0.0098	1.88
6	η_7	$16, 30, \ldots, 1598$	$0.8, 1.5, \ldots, 79.9$	0.0136	1.89
7	η_8	$7, 21, \ldots, 1589$	$0.35, 1.05, \ldots, 79.45$	0.0142	1.72
8	η_{10}	$12, 26, \ldots, 1594$	$0.6, 1.3, \ldots, 79.7$	0.0133	1.90
9	η_{13}	$17, 31, \ldots, 1599$	$0.85, 1.55, \ldots, 79.95$	0.0014	1.85
10	η_{14}	$8, 22, \ldots, 1590$	$0.4, 1.1, \ldots, 79.5$	0.0091	1.90
11	η_{18}	$13, 27, \ldots, 1595$	$0.65, 1.35, \ldots, 79.75$	0.0001	1.88
12	δ_{a_1}	$18, 32, \ldots, 1600$	$0.9, 1.6, \ldots, 80.0$	0.0001	1.90
13	δ_{a_2}	$9, 23, \ldots, 1591$	$0.45, 1.15, \ldots, 79.55$	0.0067	1.90
14	δ_{a_3}	$14, 28, \ldots, 1596$	$0.7, 1.4, \ldots, 79.8$	0.0047	1.70

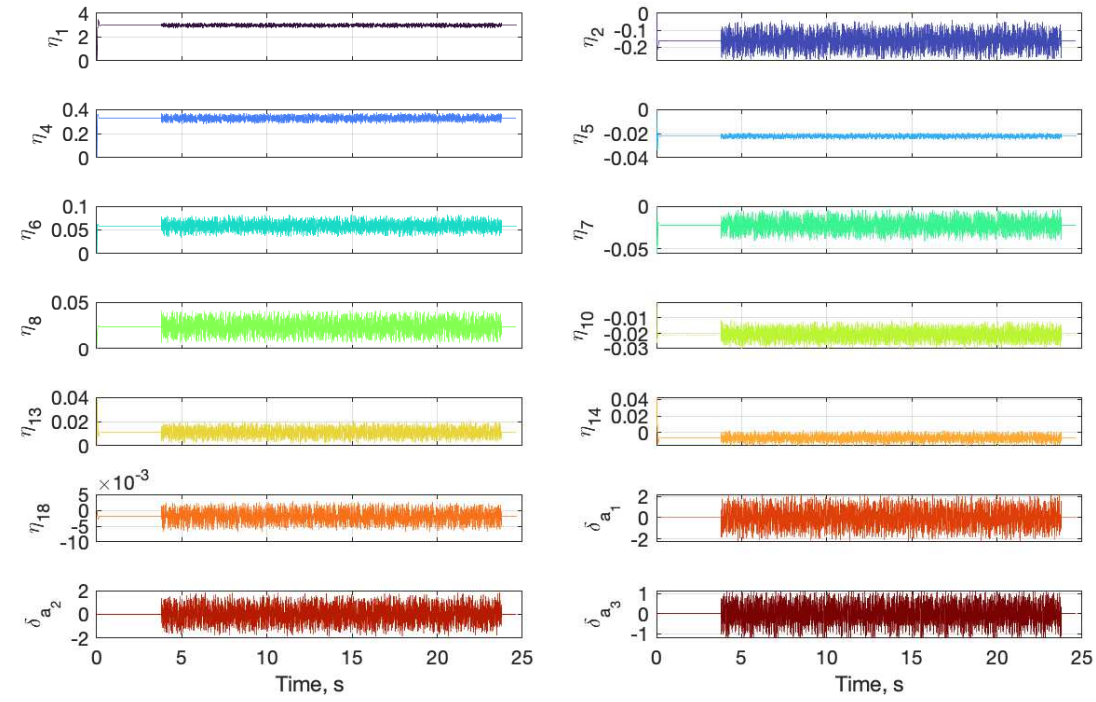

(a) Input data.

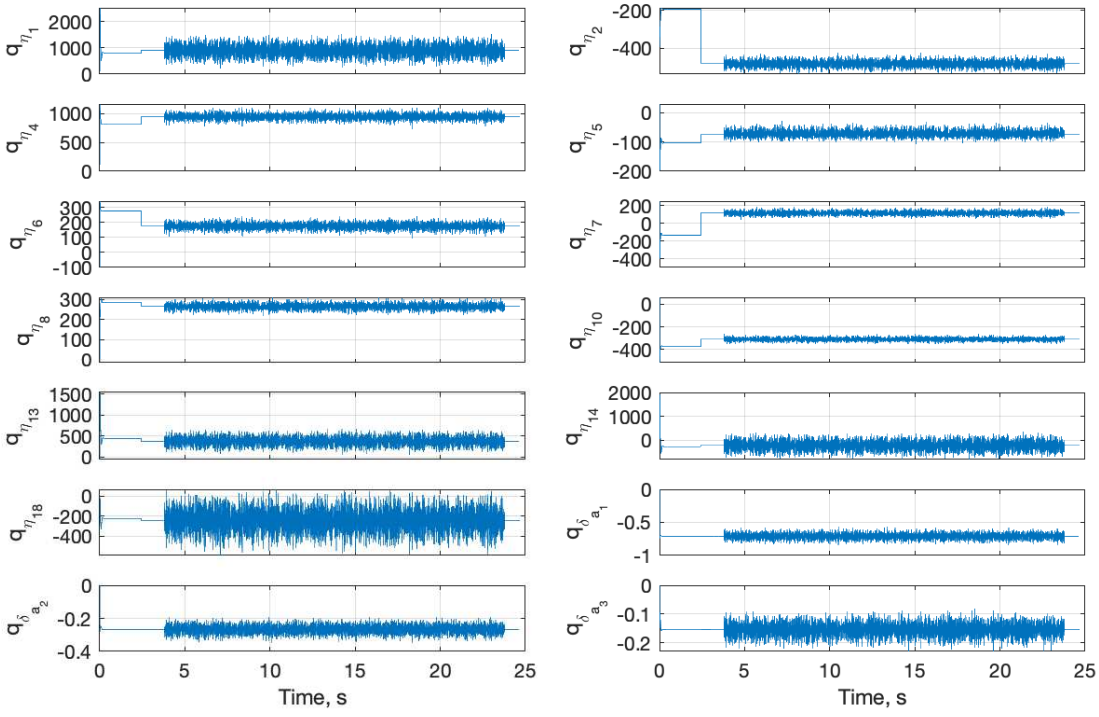

(b) Output data.

Fig. 6 Time histories of aerodynamic input and output data from FUN3D.

B. Frequency Responses

The input and output data shown in Fig. 6 were truncated between the times 3.8 and 23.8 s, over which the excitations were applied, resulting in 11802 time samples. Steady-state trim values, obtained by averaging 0.1 s (40 samples) of data just before the excitation onset, were removed from the corresponding data to obtain perturbation values.

From the perturbation time histories, Fourier transforms were computed at the 1596 harmonic frequencies. Figure 7 shows the Fourier transform magnitudes for these data. Although frequencies up to 80 Hz were analyzed, this plot is restricted to the range 0–5 Hz for clarity. Figure 7(a) illustrates that each multisine input has spectral power distributed at unique and discrete frequencies. These frequencies were chosen to be harmonics of the fundamental frequency 0.05 Hz to make the inputs mutually orthogonal.

Figure 7(b) shows the Fourier transform magnitudes of the outputs, again over the range 0–5 Hz instead of up to 80 Hz. Having inputs at distinct harmonic frequencies, assuming linearity, and applying the color coding facilitates recognizing the presence of each input frequency in this plot of the GAF responses. For example, q_{η_1} primarily contains responses due to η_1 and η_{14}, which are the dark blue and orange markers with larger amplitudes. To a lesser extent, outputs from η_2, η_{13}, δ_{a_2}, and δ_{a_3} are also present, followed by the remainder of the inputs at further lower levels.

Frequency responses were computed from each input to each output at the relevant harmonic frequencies. The entire set frequency responses is shown in Fig. 8 as a matrix of Nyquist plots. Each of these 196 frequency responses are arranged within the (14×14) matrix, where the rows correspond to the GAF outputs and the columns correspond to the structural mode displacement and control surface deflection inputs. For example, the upper-right entry, shown in dark red, is the frequency response η_1/δ_{a_3}. The colors used again indicate to the set of harmonic frequencies and follow the same scheme from Figs. 6 and 7. Because each input contains a unique set of excitation frequencies, each column of Fig. 8 uses a different color. Numbers on the plots were removed for clarity, due to the large number of frequency responses, but are included in later plots showing smaller subsets of data. The dotted lines between the 11th and 12th rows and columns distinguish between the structural mode and control surface inputs and outputs.

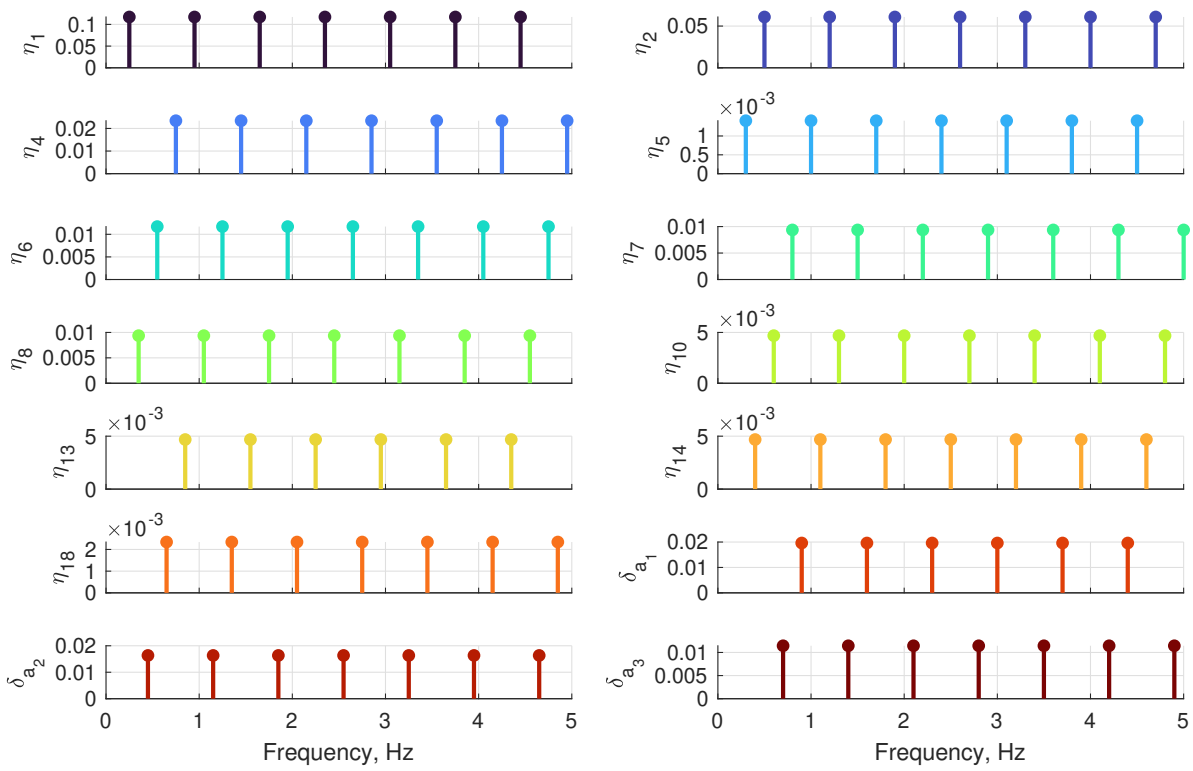

(a) Input data.

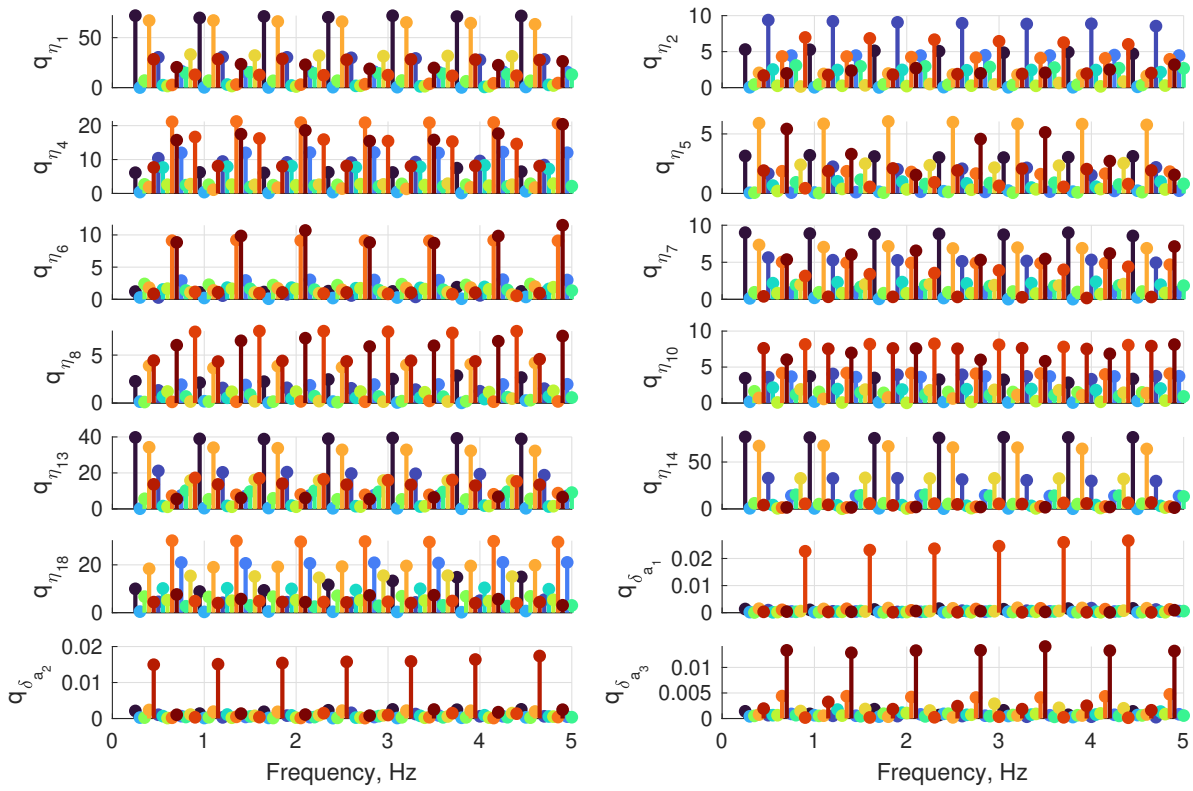

(b) Output data.

Fig. 7 Fourier transform magnitudes of input and output data over a 5 Hz subset of the 80 Hz bandwidth.

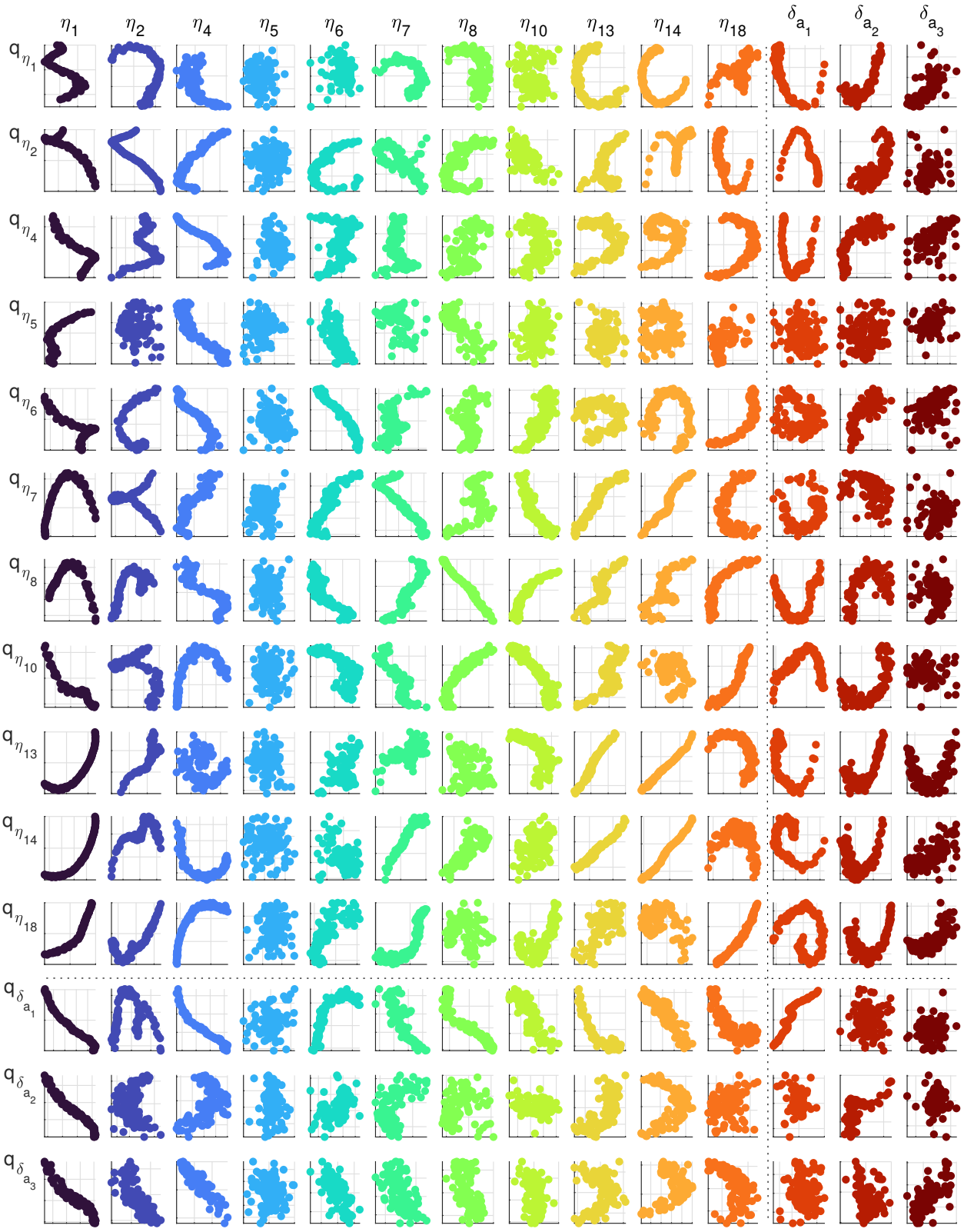

Fig. 8 GAF frequency response matrix.

C. Effects of Nonlinearity

As discussed in more detail later, many of the frequency response estimates were in agreement from predictions from other analyses. One example mentioned is the frequency response q_{η_1}/η_2. However, many of the frequency responses in Fig. 8 also had large amounts of scatter, for example most of the row corresponding to q_{η_5} or the column corresponding to δ_{a_3}.

As mentioned in Section V.C, scatter in the frequency response estimates using this technique are usually due to nonlinearities, transient responses, unmodeled inputs, and low signal-to-noise ratios where a frequency response is essentially zero. As this was a controlled simulation, unmodeled inputs and measurement noise were not factors for these data. Furthermore, analysis of the time history data, taken cycle by cycle, showed that the GAFs converged to steady-state oscillations relatively quickly and that most of the data recorded were the steady-state responses. Therefore, nonlinearity and zero transfer functions were suspected to be the sources of the scatter.

Some evidence of nonlinearity was present in the Fourier transforms. Figure 9 shows the Fourier transform magnitudes for q_{η_1} and q_{η_5}. As opposed to the analysis data and the results shown in Fig. 7, these transforms are shown for frequencies up to the 200 Hz Nyquist frequency and were computed at a finer frequency spacing of 0.02 Hz. The Fourier transform of q_{η_1} is representative of a linear system in that the output only contains power at the frequencies present in the inputs. For the multisines, the input power was at discrete frequencies up to 80 Hz. The Fourier transform of q_{η_5}, however, is characteristic of a nonlinear system in that the inputs can produce power at higher-frequency harmonics in the output.

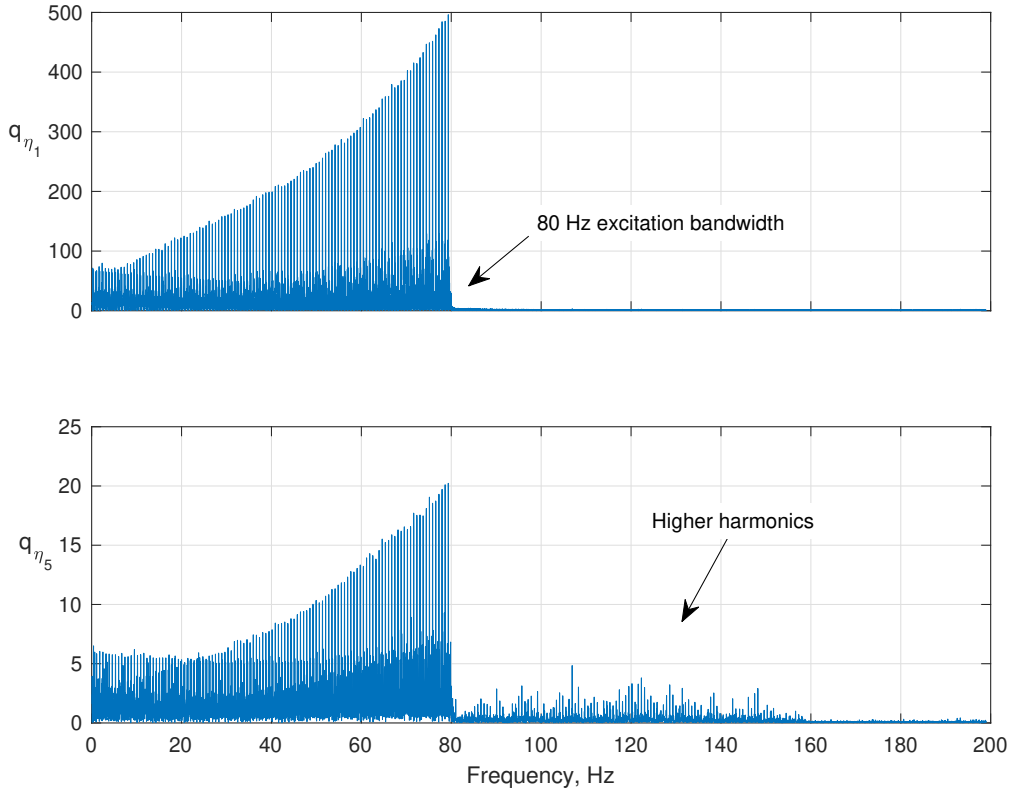

Fig. 9 Fourier transform magnitudes with and without higher-order harmonics from nonlinearity.

To examine the extent and nature of the nonlinearity, a second CFD run was performed where the control surfaces were perturbed with the same multisines but the structural modes were constrained to zero and not excited. Frequency responses for the control-on-control frequency responses from inputs δ_{a_1}, δ_{a_2}, and δ_{a_3} to outputs $q_{\delta_{a_1}}$, $q_{\delta_{a_2}}$, and $q_{\delta_{a_3}}$, are shown in Fig. 10. These plots correspond to the lower-right (3×3) submatrix of frequency responses in Fig. 8. The colored markers labeled "14 inputs" represent the frequency responses from Fig. 8 obtained from the run where all 14 inputs were excited. The white markers labeled "3 inputs" correspond to the frequency responses computed from the second CFD run where only the ailerons were excited.

In both cases, interactions between the inboard aileron with the outboard ailerons reflected in the frequency responses $q_{\delta_{a_1}}/\delta_{a_2}$, $q_{\delta_{a_1}}/\delta_{a_3}$, $q_{\delta_{a_2}}/\delta_{a_1}$, and $q_{\delta_{a_3}}/\delta_{a_1}$ were small and without a coherent structure. This was because these frequency responses were effectively zero due to the inboard aileron being separated from the outboard ailerons and without significant aerodynamic interaction.

In contrast were the frequency responses between inputs δ_{a_2} and δ_{a_3} to outputs $q_{\delta_{a_2}}$ and $q_{\delta_{a_3}}$. These frequency responses had a coherent structure but more scatter when all 14 inputs were applied relative to when only the 3 control surface deflections were excited. In comparison, the frequency response $q_{\delta_{a_1}}/\delta_{a_1}$ for the inboard aileron is almost identical between the two runs because the interactions between the structure and control surface are generally smaller and more linear.

Similar results due to the nonlinearity are evident in Fig. 11, which shows the control-on-structure frequency responses from the control surface deflection inputs to the GAF outputs for the first four retained structural modes. In Fig. 8, this corresponds to the upper-right (4×3) submatrix of frequency responses. In addition to the results from the two CFD runs, linear predictions from ZAERO, labeled "Panel code," are also shown.

The panel code predictions generally had the same structure observed from the CFD data but were in many cases scaled by a factor. This was expected because linear panel code methods generally degrade in accuracy for nonlinear flow conditions such as in the transonic flow regime. Comparison of the axis scales indicates that the outboard ailerons were generally more effective at exciting the structural modes than the inboard aileron, as expected.

In general, the frequency responses computed from the run with only the 3 inputs had less scatter than those from the run with 14 inputs due to the presence of nonlinear interactions between the structure and control surfaces. The scatter was larger for the outboard ailerons than for the inboard aileron because the wing deflections are generally larger near the wing tip. All frequency responses from input η_5 and many frequency responses from inputs η_4 and η_6 contained this scatter, which indicated nonlinear interactions. Note that Ref. [11] identified these structural modes as participating most heavily in the flutter mechanisms. Due to modeling errors and the presence of nonlinearity, control laws for AFS based on panel code predictions may therefore have poor closed-loop performance at this transonic condition.

Figure 12 shows a subset of structure-on-structure frequency responses from the first three retained structural modes to the corresponding GAFs. In Fig. 8, this corresponds to the upper-left (3×3) submatrix of frequency responses. In Fig. 12, the results from the CFD run with 14 inputs are again shown with the panel code predictions. In addition, results are shown in magenta and labeled as "LFD" for a linearized frequency domain [32] analysis on the FUN3D code. The LFD results are obtained by linearizing the governing equations for the flow about the nonlinear static aeroelastic CFD solution to achieve computational cost savings over the standard time-marching approach. The resulting GAFs from the LFD solution include some nonlinearity in the mean flow that the linear panel solutions do not.

Similar trends were seen between the frequency responses computed by the FUN3D run with 14 inputs and the panel code predictions in that the same structure was present but a scale factor difference was evident. At low reduced frequencies, the LFD results generally agreed with those for the CFD run with 14 inputs. However, for many input-output pairs and frequencies above about 24 Hz (reduced frequency of 0.35), the LFD results departed and generally tended towards the panel code results as frequencies increased. As the LFD method can account for some nonlinearity, this departure may suggest that nonlinearities above 24 Hz are more significant in the responses for some input-output pairs.

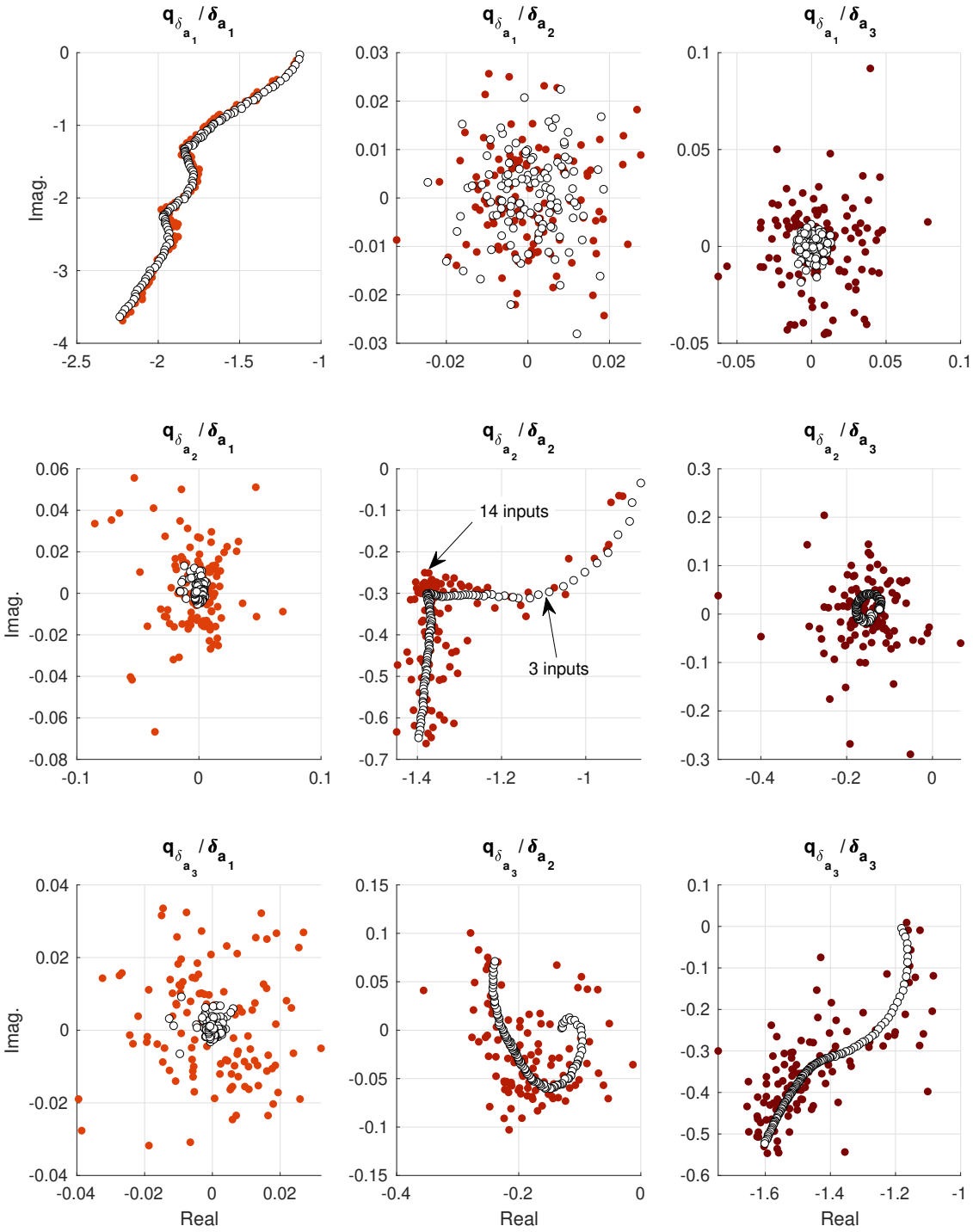

Fig. 10 Control-on-control frequency responses showing effects of zero transfer functions and nonlinearities.

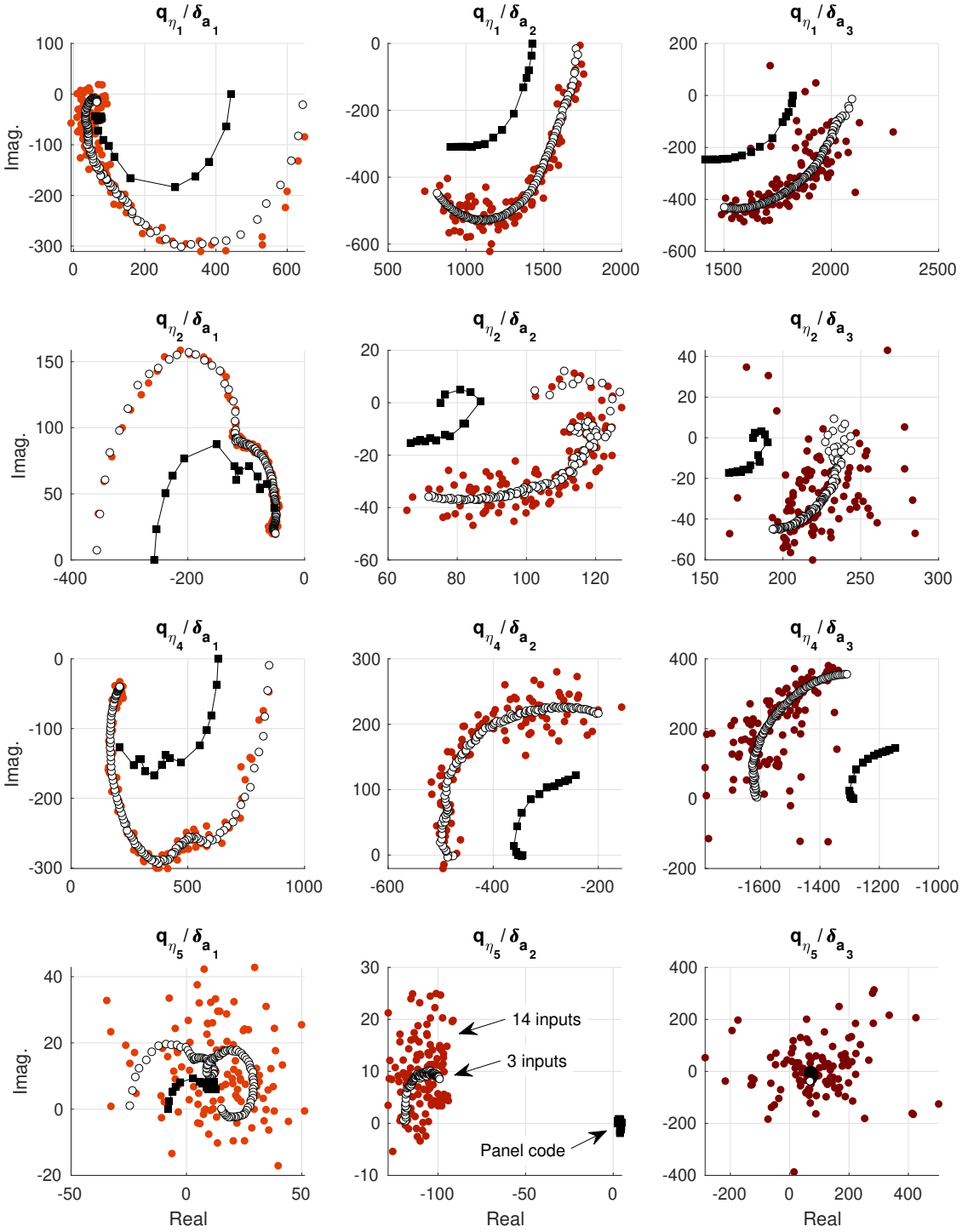

Fig. 11 Subset of control-on-structure frequency responses showing effects of nonlinearities.

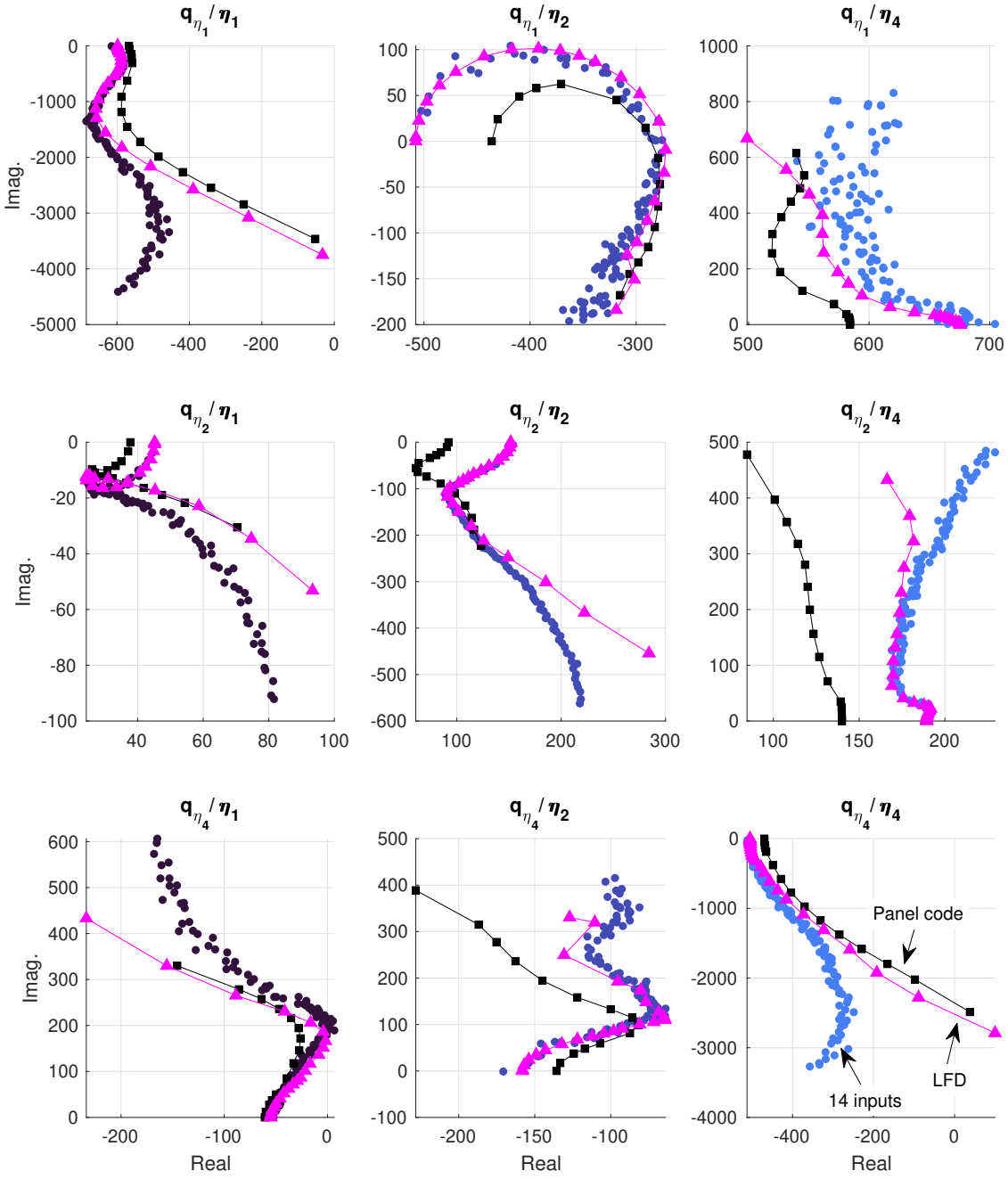

Fig. 12 Subset of structure-on-structure frequency responses.

D. Parameter Estimation

The frequency responses from the CFD runs using all 14 inputs were fit with RFAs of the form in Eq. (6). Six aerodynamic lags were included between reduced frequencies of 0.1 – 1.1 and spaced in 0.2 increments (corresponding to dimensional frequencies between 6.8 – 75 Hz in 13.7 Hz increments). Although different numbers and locations for the aerodynamic lags could have been assigned for each frequency response, these roots were used in all cases for simplicity. Fits to the frequency domain data are shown as solid black lines in Fig. 13, which is arranged similarly to Fig. 8. Most of the fits had high coefficients of determination R^2, up to 0.9998, which indicated an excellent match to the data. However, frequency responses having nonlinearities present had lower fit quality, down to R^2 values of 0.01, due to the increased scatter.

Fits to the upper-left (3×3) submatrix of structure-on-structure frequency responses in Fig. 13 are shown with more detail in Fig. 14. The colored markers labeled "Data" are the frequency response estimates and the solid line labeled "RFA model" are the fits. For these input-output pairs, the RFA models were excellent approximations of the computed frequency responses and had values of R^2 above 0.992. However, model structure errors remained in q_{η_4}/η_2, which could be improved by increasing the number of aerodynamic lags in the RFA for that frequency response.

Fits to the lower-right (2×2) submatrix of control-on-control frequency responses in Fig. 13, from the δ_{a_2} and δ_{a_3} control surface deflections to the corresponding GAFs, are shown in Fig. 15. In this plot, the black solid line represents the RFA fit to the frequency response data from the CFD run with 14 inputs. The frequency response data from the CFD run with 3 inputs are also shown, with the corresponding RFA fit shown as the green line. The two RFA fits are similar in shape but differ due to the increased scatter in the frequency responses from the CFD run with 14 inputs. Parameter estimates with ±2 standard error uncertainty bounds are shown in Fig. 16 for both sets of results. The fits for the CFD run having 3 inputs had higher R^2 values and lower estimated standard errors for the model parameters.

For these reasons, better models would result for this flow condition and using these frequency response methods when two separate CFD runs are made, one with structural mode inputs and one with control surface inputs. This reduces the nonlinear interactions and produces frequency responses with less scatter, which then results in more accurate RFA fits for use in the ASE state-space models. However, blocking the inputs in this way doubles the amount of computation time needed to run the CFD solver, which is significant.

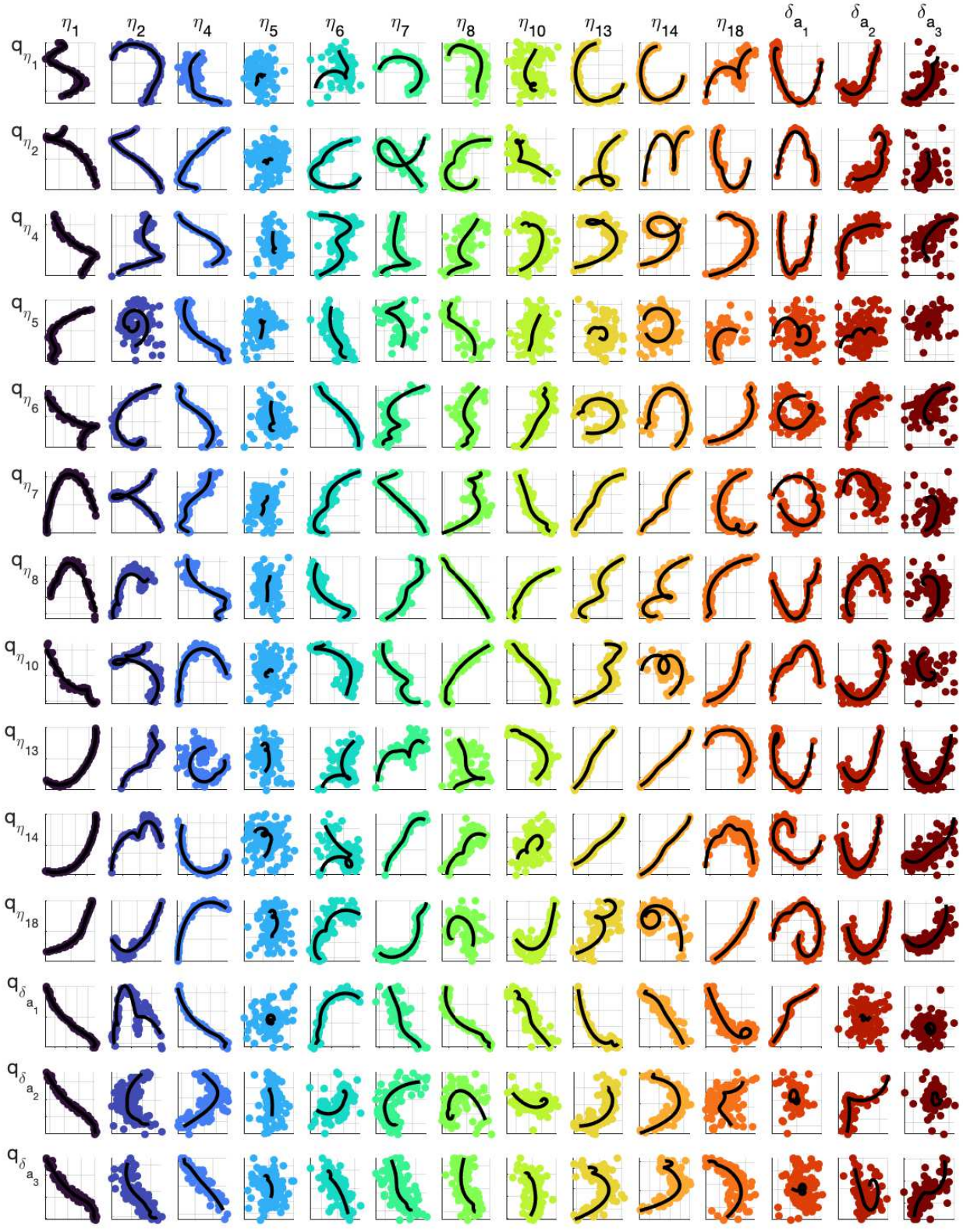

Fig. 13 GAF frequency response matrix (colored markers) and RFA fits (solid black line).

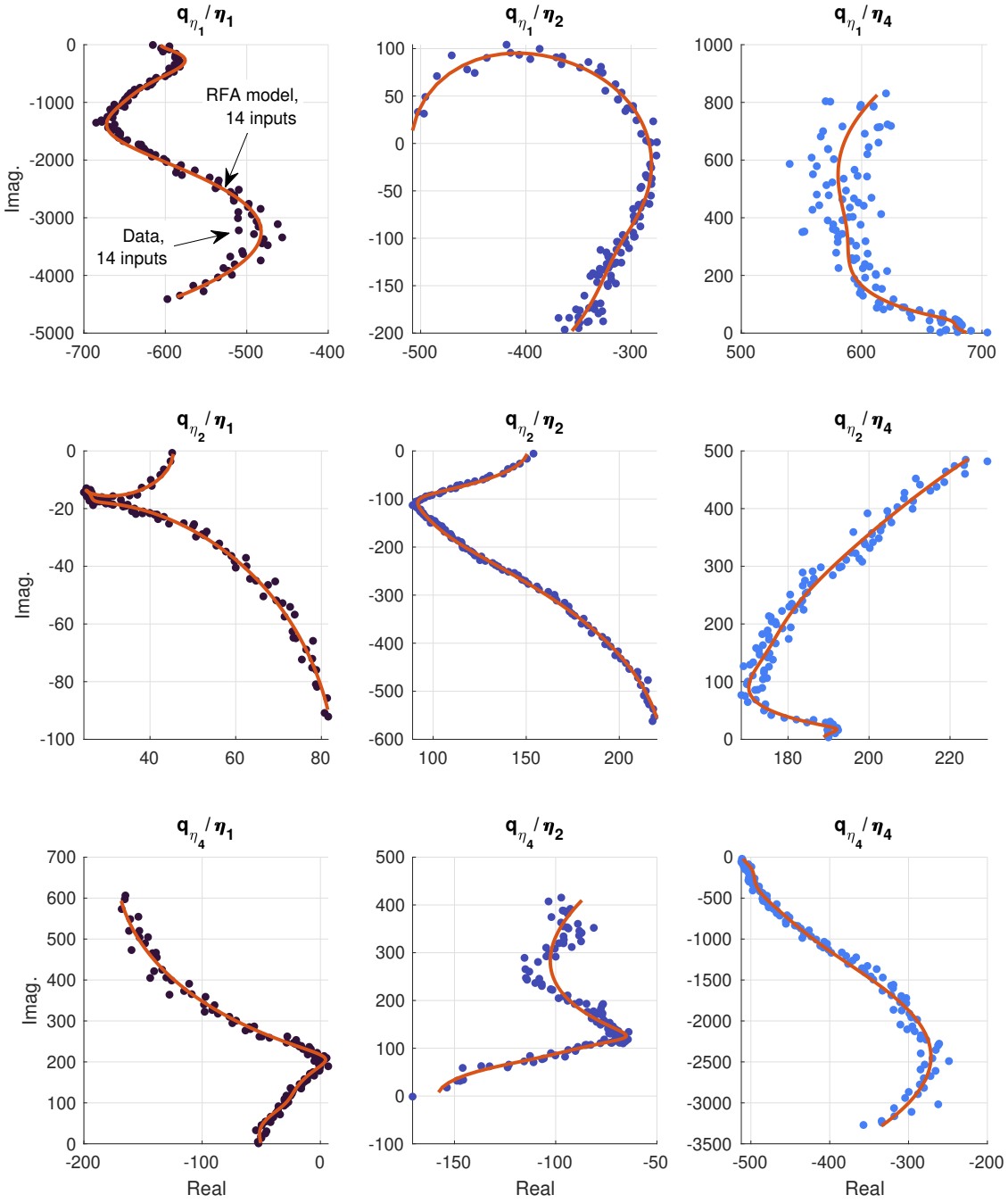

Fig. 14 Rational function approximation fits to a subset of structure-on-structure frequency responses.

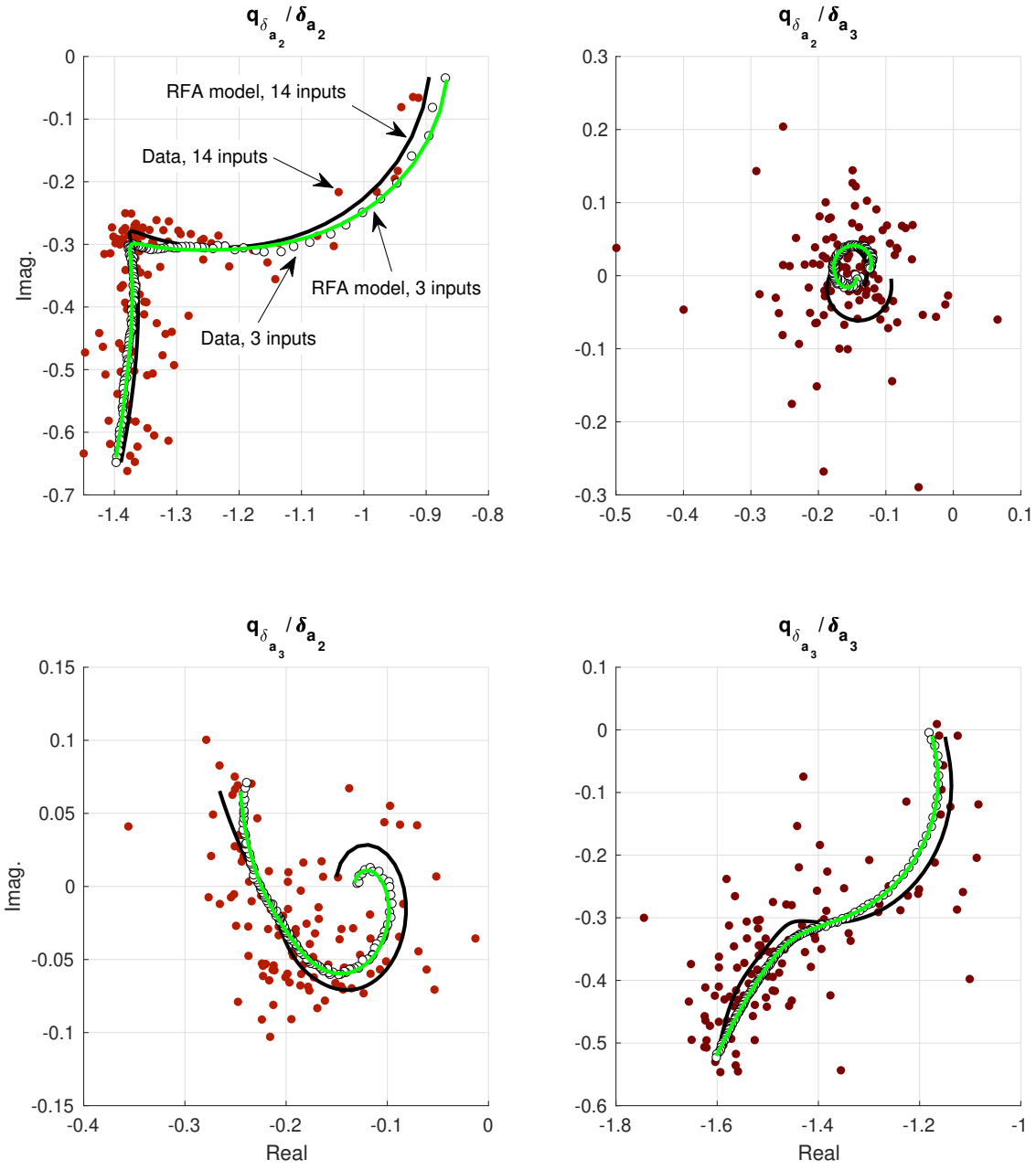

Fig. 15 Rational function approximation fits to a subset of control-on-control frequency responses.

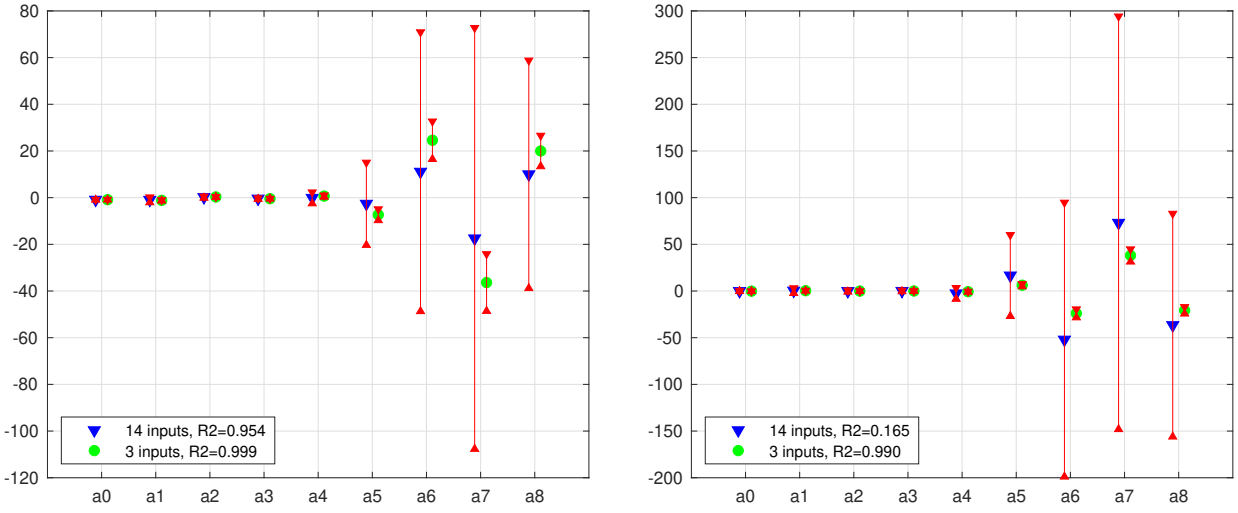

(a) $q_{\delta_{a_2}}/\delta_{a_2}$.

(b) $q_{\delta_{a_2}}/\delta_{a_3}$.

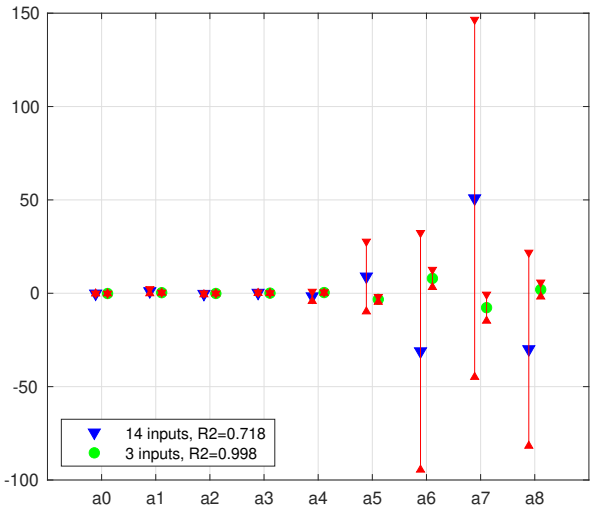

(c) $q_{\delta_{a_3}}/\delta_{a_2}$.

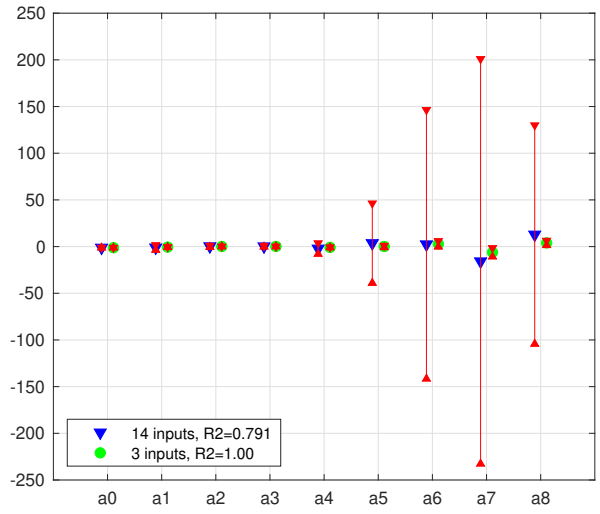

(d) $q_{\delta_{a_3}}/\delta_{a_3}$.

Fig. 16 Estimated RFA parameters with ±2 standard error uncertainty bounds.

VII. Conclusions

A system identification analysis was performed on a computational fluid dynamics (CFD) solver configured for the Integrated Adaptive Wing Technology Maturation (IAWTM) project in the transonic flow regime. The wind tunnel test article is a half-span model with significant aeroelastic interactions. The CFD inputs included 14 retained structural modes and 3 aileron control surface deflections, whereas the outputs were generalized aerodynamic forces (GAFs) acting on the structural dynamics and actuator dynamics. The system identification approach included trimming the flow solver, applying orthogonal multisine inputs to the inputs, computing Fourier transforms from input-output perturbation data, and fitting rational function approximations (RFAs) using least squares.

The main findings in this work were the following:

1) It was possible to compute the entire (14×14) matrix of 196 frequency responses from a single CFD run with 20 s of excitation. Using orthogonal multisines saved expensive computation time over other inputs that must be applied sequentially one at a time, particularly for systems with multiple inputs such as the IAWTM. Using this method of frequency response estimation was computationally efficient and simplified the data processing step. Moreover, it was based directly on the recorded input-output data and did not require any analyst judgement or tuning. However, a lower-fidelity but readily available aeroservoelastic (ASE) model based on panel method results from ZAERO was used to determine amplitudes of the multisine perturbations for the structural modes.
2) In the presence of input-output nonlinearities, which were expected in this transonic flow condition, the frequency response estimates degraded gracefully, manifesting as increased scatter. The scatter diminished when only the control surface inputs were excited, during a second CFD run, which added further evidence to previous experience of nonlinear interactions between the structural modes and control surfaces. Discrepancies between the results and a previous CFD analysis using the linearized frequency domain (LFD) method for some frequency responses above 24 Hz (reduced frequency 0.35) and for the outboard section of the wing were observed but require further investigation.
3) At the expense of additional computation time, nonlinearities can be reduced by performing one CFD run where only the structural mode displacements were excited, and a second CFD run where only the control surfaces were excited. This blocking of the inputs reduces the scatter of the frequency responses, which can lead to potentially smaller and more accurate rational function approximations (RFAs) for use in the state-space aeroservoelastic (ASE) models.

Future work is planned to further investigate the sources of nonlinearity discussed in this work. In addition, more complete verifications of the modeling accuracy, based on ASE models constructed using the CFD aerodynamics and identified reduced-order models, will be examined. Wind tunnel tests in the NASA Langley Research Center (LaRC) Transonic Dynamics Tunnel (TDT) for system identification and feedback control applications are scheduled for the year 2021.

Acknowledgments

This research was supported by the NASA Advanced Air Transport Technology (AATT) Project. The contributions by the IAWTM team members at NASA Langley Research Center, Boeing Research and Technology, and NextGen Aeronautics are gratefully acknowledged. Robert Bartels provided static aeroelastic solutions for the FUN3D CFD solver. Technical discussions with Jeffrey Ouellette and Walter Silva are acknowledged and appreciated.

References

[1] Raveh, D., "Reduced-Order Models for Nonlinear Unsteady Aerodynamics," *AIAA Journal*, Vol. 39, No. 8, 2011, pp. 1417–1429. doi:10.2514/2.1473.

[2] Silva, W., and Bartels, R., "Development of Reduced-Order Models for Aeroelastic Analysis and Flutter Prediction Using the CFL3Dv6.0 Code," *Journal of Fluids and Structures*, Vol. 19, No. 6, 2004, pp. 729–745. doi:10.1016/j.jfluidstructs.2004.03.004.

[3] Raveh, D., "Identification of Computational-Fluid-Dynamics Based Unsteady Aerodynamic Models for Aeroelastic Analysis," *Journal of Aircraft*, Vol. 41, No. 3, 2004, pp. 620–632. doi:10.2514/1.3149.

[4] Silva, W., "Simultaneous Excitation of Multiple-Input/Multiple-Output CFD-Based Unsteady Aerodynamic Systems," *Journal of Aircraft*, Vol. 45, No. 4, 2008, pp. 1267–1274. doi:10.2514/1.34328.

[5] Silva, W., Vatsa, V., and Biedron, R., "Development of Unsteady Aerodynamic and Aeroelastic Reduced-Order Models Using the FUN3D Code," IFASD Paper 2009-030, 2009.

[6] Silva, W., "AEROM: NASA's Unsteady Aerodynamic and Aeroelastic Reduced-Order Modeling Software," *Aerospace*, Vol. 5, No. 41, 2018, pp. 1–18. doi:10.3390/aerospace5020041.

[7] Juang, J., *Applied System Identification*, Prentice Hall, Upper Saddle River, NJ, 1994.

[8] Zona Technology Inc., "ZAERO v.9.3 Theoretical Manual," , January 2019.

[9] Biedron, R., et al., "FUN3D Manual: 13.6," NASA TM-2019-220416, October 2019.

[10] Lee-Rausch, B., "FUN3D," `http://fun3d.larc.nasa.gov`, accessed May 2020.

[11] Waite, J., Bartels, R., and Stanford, B., "Aeroelastic Model Development for the Integrated Adaptive Wing Technology Maturation Project Wind-Tunnel Test," AIAA Paper 2020-2717, 2020. doi:10.2514/6.2020-2717.

[12] Waite, J., Grauer, J., Bartels, R., and Stanford, B., "Aeroservoelastic Control Law Development for the Integrated Adaptive Wing Technology Maturation Project Wind-Tunnel Test," to be published, 2021.

[13] Gipson, L., "Advanced Air Transport Technology (AATT) Project Technical Challenges," `http://www.nasa.gov/aeroresearch/programs/aavp/aatt/technical-challenges/`, accessed May 2020.

[14] Heaney, P., Ivanco, T., and Bilgen, O., "Distributed Sensing of a Cantilever Beam and Plate using a Fiber Optic Sensing System," AIAA Paper 2018-3482, 2018. doi:10.2514/6.2018-3482.

[15] Grauer, J., "Method for Real-Time State Estimation of Structural Modes for an AeroelasticWind Tunnel Model," (to be published), 2021.

[16] Brooks, T., Kenway, G., and Martins, J., "Benchmark Aerostructural Models for the Study of Transonic Aircraft Wings," *AIAA Journal*, Vol. 56, No. 7, 2018, pp. 2840–2855. doi:10.2514/1.J056603.

[17] Peele, E., and Adams, W., "A Digital Program for Calculating the Interaction Between Flexible Structures, Unsteady Aerodynamics, and Active Controls," NASA TM-80040, January 1979.

[18] Adams, W., and Hoadley, S., "ISAC: A Tool for Aeroservoelastic Modeling and Analysis," AIAA Paper 1993-1421, 1993. doi:10.2514/6.1993-1421.

[19] Buttrill, C., Bacon, B., Heeg, J., Houck, J., and Wood, D., "Simulation and Model Reduction for the Active Flexible Wing Program," *Journal of Aircraft*, Vol. 32, No. 1, 1995, pp. 23–31. doi:10.2514/3.46679.

[20] Buttrill, C., Bacon, B., Heeg, J., and Houck, J., "Aeroservoelastic Simulation of an Active Flexible Wing Wind Tunnel Model," NASA TP-3510, April 1996.

[21] Karpel, M., and Strul, E., "Minimum-State Unsteady Aerodynamic Approximations with Flexible Constraints," *Journal of Aircraft*, Vol. 33, No. 6, 1996, pp. 1190–1196. doi:10.2514/3.47074.

[22] Roger, K., "Airplane Math Modeling Methods for Active Control Design," AGARD-CP-228, August 1977.

[23] Tiffany, S., and Adams, W., "Fitting Aerodynamic Forces in the Laplace Domain: An Application of a Nonlinear Nongradient Technique to Multilevel Constrained Optimization," NASA TM-86317, October 1984.

[24] Tiffany, S., and Adams, W., "Nonlinear Programming Extensions to Rational Function Approximation Methods for Unsteady Aerodynamic Forces," NASA TP-2776, July 1988.

[25] Tiffany, S., and Karpel, M., "Aeroservoelastic Modeling and Applications Using Minimum-State Approximations of the Unsteady Aerodynamics," AIAA Paper 89-1188, 1989. doi:10.2514/6.1989-1188.

[26] Morelli, E., "System IDentification Programs for AirCraft (SIDPAC)," version 4.1, NASA Software Catalog, `http://software.nasa.gov`, accessed May 2020.

[27] Morelli, E., and Klein, V., *Aircraft System Identification: Theory and Practice*, 2nd ed., Sunflyte, Williamsburg, VA, 2016.

[28] Grauer, J., and Boucher, M., "Aircraft System Identification from Multisine Inputs and Frequency Responses," *Journal of Aircraft*, Vol. 43, No. 12, 2020, pp. 2391–2398. doi:10.2514/1.G005131.

[29] Heeg, J., and Morelli, E., "Evaluation of Simultaneous Multisine Excitation of the Joined Wing SensorCraft Aeroelastic Wind Tunnel Model," AIAA Paper 2011-1959, 2011. doi:10.2514/6.2011-1959.

[30] Heeg, J., and Wieseman, C., "System Identification and Uncertainty Quantification Using Orthogonal Excitations and the Semi-Span SuperSonic Transport (S^4T) Model," AIAA Paper 2012-1404, 2012. doi:10.2514/6.2012-1404.

[31] Grauer, J., and Boucher, M., "System Identification of Flexible Aircraft: Lessons Learned from the X-56A Phase 1 Flight Tests," AIAA Paper 2020-1017, 2020. doi:10.2514/6.2020-1017.

[32] Jacobson, K., Stanford, B., Wood, S., and Anderson, K., "Flutter Analysis with Stabilized Finite Elements Based on the Linearized Frequency-Domain Approach," AIAA Paper 2020-0403, 2020. doi:10.2514/6.2020-0403.